



# Highly photoactive Brookite and Anatase with enhanced photocatalytic activity for the degradation of indigo carmine application



Jesús Adrián Díaz-Real<sup>a,b</sup>, Jiwei Ma<sup>a,c</sup>, Nicolas Alonso-Vante<sup>a,\*</sup>

<sup>a</sup> JC2MP, UMR-CNRS 7285, Université de Poitiers, 4 rue Michel Brunet, F-86073 Poitiers, France

<sup>b</sup> Centro de Investigación y Desarrollo Tecnológico en Electroquímica, Pedro Escobedo, Qro., C.P. 76703, Mexico

<sup>c</sup> Faculty of Materials Science and Engineering, Hubei University, 430062 Wuhan, China

## ARTICLE INFO

### Article history:

Received 1 April 2016

Received in revised form 29 May 2016

Accepted 2 June 2016

Available online 3 June 2016

### Keywords:

Brookite

Anatase

Photoactivity

Degradation

Indigo carmine

Photo-electrochemical microreactor

## ABSTRACT

TiO<sub>2</sub> Brookite, and Anatase powders were prepared by a facile and low temperature solution based method. XRD diffractometry was performed to confirm their phase composition and crystallinity. Morphology was further confirmed by TEM. N<sub>2</sub> adsorption was used to determine surface area and pore size distribution. The difference in capacitive properties of both materials and the determination of the flat band position was obtained by Mott-Schottky analysis. Diffuse reflectance and Tauc plots allowed to obtain the band gap value. The degradation of Indigo Carmine dye with both catalysts in a photo-electrochemical microreactor was assessed by UV-vis, and Raman spectroscopy. Both materials were more active than the benchmark commercial Degussa P25 sample in the order P25 < Anatase < Brookite and explained in terms of energy band positions.

© 2016 Elsevier B.V. All rights reserved.

## 1. Introduction

Titanium dioxide (TiO<sub>2</sub>) is a sophisticated material of interest for multiple ranges of applications due to its intrinsic semiconducting properties, high resistance to corrosion, low toxicity and low cost. It has been used in a wide spectrum of applications like cosmetics, coatings, sensors, dye-sensitized solar cells (DSSC), photocatalysis and batteries [1]. The commonly natural polymorphs of TiO<sub>2</sub> found are rutile (P4<sub>2</sub>/mnmm), Anatase (I4<sub>1</sub>/amd) and Brookite (Pbca) [2]. These different crystal structures directly affect the electronic and surface properties of each of the polymorphs. The principal investigated polymorphs of TiO<sub>2</sub> are Rutile and Anatase while less explored are the properties of Brookite, and this is mainly due to the difficulty to obtain Brookite in pure form as reflected in the number of studies on this material that are not as abundant as other crystalline phases [3]. This condition has produced many reports centered in the preparation procedure to propose a formation mechanism [4–11].

At laboratory conditions, Brookite has been synthesized by various approaches, such as hydrothermal [12,13], aqueous

precipitation/sol-gel [14–17], and template-assisted [18] methods. A widely used chemical technique for the preparation of Brookite powders is the hydrothermal method but it faces an inherent lack of crystalline phase selectivity [4]. Often mixtures of phases are found during syntheses processes if parameters are not carefully maintained and in the vast majority of data, the literature reports traces of the other two phases. Indeed, the factors that determine the specific formation of Brookite phase are hard to predict (precursor, pH, reagent ratios, temperature or pressure) and thus, the information obtained from one particular methodology is not easily transferable to other approaches. Therefore, it is clear that one of the most difficult challenges is to achieve pure crystalline Brookite.

Another greatly desirable characteristic in TiO<sub>2</sub> is to attain a high surface area which is demanded from most of the current nanotechnological applications. For instance, in DSSC and batteries the porosity and the surface area are linked directly to the electrochemical kinetics and electron diffusion pathways that greatly determine the performance of the final devices [19]. The gain of control in the morphology and surface area of the nanostructures allows the tunability of the electronic and structural properties of these materials and such a reason has attracted many efforts [12,19–23].

As previously mentioned, a major issue to study systematically the photocatalytic properties of the single crystalline phase are related to the phase purity. The understanding of the energetics

\* Corresponding author.

E-mail address: [nicolas.alonso.vante@univ-poitiers.fr](mailto:nicolas.alonso.vante@univ-poitiers.fr) (N. Alonso-Vante).

of  $\text{TiO}_2$  materials is of great importance, and therefore the determination of the band gap and flat band values. However, many experimental approaches found in the literature occur in great disagreement either in optical or electronic values for Brookite since their results are obtained from Brookite samples not entirely crystalline. On the other hand, several computational studies based in density functional theory (DFT) have been done for Anatase and Rutile, while for Brookite are not as often. The new approaches for this crystalline phase bring interesting information that should be considered by work-groups to confirm with their experimental values [24].

The photocatalytic activity of Brookite has been, however, undertaken in several applications. DSSC cells have been prepared using pure Brookite and compared with Anatase demonstrating that the former is a promising material and that the performance of the cells greatly depends also on the morphology of the materials [25]. In hydrogen evolution, thin films of mixed-phase Anatase and Brookite were prepared and assessed under visible light irradiation [26] and nanorods were used in aqueous methanol solutions [21]. The modification of Brookite powders with Pt nanoparticles have been also used in the photocatalytic dehydrogenation of 2-propanol [27]. The photodegradation of organic molecules has been reported for chlorophenol [22] and acetaldehyde [28], rhodamine B [29–31], but, all these reports showed lower performances when compared with Anatase phase. However, when hollow-templated Brookite structures were assessed with the same rhodamine B, the degradation activity was enhanced and explained in terms of the increased exposed area [32]. This same explanation was given when the degradation of dichloroacetic acid was assessed using Brookite nanorods and were less active than Anatase, but more active than P25 when used in the degradation of phenol [33]. On the other hand, Brookite nanoflowers were evaluated in the degradation of methyl orange and exhibited higher activity than Anatase and Anatase/Brookite mixtures in spite of having a lower specific surface area [12,23]. Nevertheless, the influence of the crystalline planes determined markedly the photoactivity of Brookite nanorods as observed with the improved degradation of toluene after performing a chemical etching [13].

Although some studies have been done to explain the origin of an improved photoactivity of Brookite catalysts, the characterization approaches: physicochemical and electro-chemical, are seldom observed in the same report [3]. In this work, low temperature solution-based syntheses were used to produce Brookite and Anatase powders possessing similar surface area, which were used to produce photoelectrodes by spin-coating technique. The influence of the deposited mass was studied in the photo-electrochemical responses and used to understand the energetics for each material. Finally, a home-made photo-electrochemical microreactor was used to perform the degradation of potassium carmine indigo trisulfonate (InC) under UV-vis irradiation.

## 2. Experimental

### 2.1. Preparation of $\text{TiO}_2$ Anatase and Brookite materials

The synthesis process of  $\text{TiO}_2$  Anatase consisted of thermolysis of titanium oxysulfate (Sigma Aldrich) in an aqueous solution, followed with a post-heat treatment [20]. Briefly, titanium oxysulfate was firstly dissolved in ultrapure water with a concentration of 0.9 M by slightly heating to 90 °C. The precipitation of  $\text{TiO}_2$  is then obtained by heating the solution at 90 °C for 4 h. The powder is recovered by filtration, and washed with ultrapure water.  $\text{TiO}_2$  Anatase was further obtained by post-heat treatment at 400 °C for 2 h under air atmosphere. Secondly, to prepare  $\text{TiO}_2$  Brookite, the synthesis was performed with anionic species, i.e., lithium

oxalate (Sigma Aldrich), followed by a post-heat treatment process [19]. Briefly, titanium and lithium salts were dissolved simultaneously in the ultrapure water by slightly heating to 90 °C. The molar ratio between titanium and the oxalate group was fixed at 1. Titanium oxalate hydrate,  $\text{Ti}_2\text{O}_3(\text{H}_2\text{O})_2(\text{C}_2\text{O}_4)\cdot\text{H}_2\text{O}$ , was firstly obtained by the precipitation process at 90 °C for 4 h. The precipitated powder was recovered by filtration, and washed with a large amount of ultrapure water, and dried at 80 °C overnight. Thereafter,  $\text{TiO}_2$  Brookite was obtained by thermal decomposition of  $\text{Ti}_2\text{O}_3(\text{H}_2\text{O})_2(\text{C}_2\text{O}_4)\cdot\text{H}_2\text{O}$  at 400 °C for 2 h under air atmosphere.

### 2.2. Electrode preparation

The photo-electrodes were prepared by spin-coating technique with a home-made device. The suspensions were prepared with a concentration of 15 mg/mL of each of  $\text{TiO}_2$  material in ethanol. An addition rate of 60  $\mu\text{L}/\text{min}$  with a rotating speed of 1800 rpm were used to drop-cast over a conducting glass substrate (SOLEMS, FTO 20  $\Omega$ ). After spin-coating, a thermal annealing was performed at 400 °C (10 °C/min, 1 h) under air. Electrical contact to the FTO was done with silver conducting paint (RadioSpares, 186-3593) to a copper wire and isolated with epoxy resin (3 M, Scotch-weld DP-190).

### 2.3. Physicochemical characterization

XRD measurements of  $\text{TiO}_2$  powders were carried out on an EMPYREAN PANALYTICAL X-ray diffractometer using Cu-K $\alpha$  radiation ( $\lambda = 0.15406 \text{ nm}$ ). The XRD spectra were obtained using high resolution with the step-scanning mode, a narrow receiving slit (1/16°), and a counting time of 240 s per 0.05°. Scans were recorded in the range of 20°–90°. The identification of the phases was made with reference to the Joint Committee on Powder Diffraction Standards International Center for Diffraction Data (JCPDS-ICDD) database.

The morphology of particles was examined by TEM on a JEOL JEM-2001 equipped with a LaB<sub>6</sub> filament. The samples were characterized under an accelerating voltage of 200 kV and a resolution of ca. 0.19 nm.

Nitrogen adsorption isotherms were recorded at 77 K on a Micromeritics ASAP 2020 device. The specific surface area and pore size distribution were calculated using the Brunauer–Emmett–Teller (BET) and Barrett–Joyner–Halenda (BJH) methods, respectively.

Diffuse reflectance was performed with a spectrophotometer (Cary 5000, VARIAN) from 200 to 800 nm with an interval of 1 nm. A BaSO<sub>4</sub> spectrum was used, in the spectral range, as blank.

### 2.4. Photo-electrochemical characterization

Electrochemical measurements were performed with a galvanostat/potentiostat (Biologic, SP300) in a cell provided with a quartz window facing the working electrode through which it was illuminated. A N<sub>2</sub>-saturated 0.5 M H<sub>2</sub>SO<sub>4</sub> was used as supporting electrolyte. A glassy carbon and RHE were used as counter and reference electrode, respectively. Cyclic voltammetry was performed to stabilize current density after 20 cycles ( $v = 100 \text{ mV/s}$ ). Linear sweep voltammetry (LSV) were performed ( $v = 5 \text{ mV/s}$ ) to obtain photo-current values,  $J_{ph}$ . Photo-current transients (at a  $v = 5 \text{ mV/s}$ ) were obtained by light chopping (Lambda SC shutter controller) with on-off periods of 5 s. Action spectra were recorded by polarizing at 1.0 V vs RHE and recorded under UV-vis illumination with

a 175 W Xenon lamp (Spectral products, ASB-XE-175EX) with an incident irradiation power at the electrode of  $5 \text{ mW/cm}^2$ .

## 2.5. Dye degradation in photo-reactor

The photocatalytic activity of the samples was evaluated in a home-made micro-fluidic electrochemical reactor. This system comprises a chamber of nine channels ( $700 \mu\text{m}$  wide and deep  $\times 1 \text{ cm}$  long) for homogeneous distribution of a  $3.5 \times 10^{-4} \text{ M}$  potassium carmine indigo trisulfonate in  $0.5 \text{ M K}_2\text{SO}_4$  in direct contact with an effective area of  $0.63 \text{ cm}^2$  of the assessed catalytic material supported and annealed in FTO. In the following, the use of the word degradation refers to the breakdown of the chromophore part of the dye, without implying complete mineralization. The reactor was kept at a constant flow of  $12.1 \text{ mL/min}$  with a micro-pump that recirculated a total volume of  $3 \text{ mL}$ . Simultaneously, UV-vis light was irradiated with an incident power  $I_0 = 34.0 \text{ mW/cm}^2$  with the same lamp used for photo-electrochemical measurements for a period of 180 min. A saturated calomel electrode and a glassy carbon were used as reference and counter-electrode, respectively, for a three-electrode configuration. The counter-electrode was maintained out of the reactor in a reservoir. This allowed the polarization of the electrode to evaluate the influence of the applied potential in the degradation rate. The absorbance of the solution was determined at  $603 \text{ nm}$  with a UV-vis spectrophotometer (PIR Varian, Cary 5000). Additionally, Raman spectra were recorded for solutions after irradiation using a LabRAM HR Evolution microscope Horiba Jobim Yvon equipped with a  $780 \text{ nm}$  laser. The incident laser,  $I_0$ , was  $4.5 \text{ mW}$  for all the samples. The recorded response was averaged from a total of 200 acquisitions in a spectral range of  $200\text{--}2000 \text{ cm}^{-1}$ .

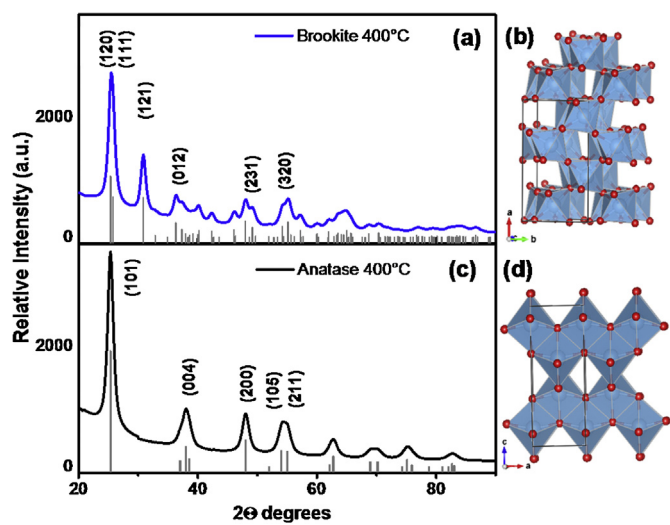


**Fig. 1.** XRD patterns for  $\text{TiO}_2$  (a) Anatase, and (c) Brookite samples after heat-treated at  $400^\circ\text{C}$ . Crystalline structure, rendered in polyhedron model of (b) Brookite and (d) Anatase.

## 3. Results and discussion

### 3.1. Physicochemical characterization

The samples were characterized by means of XRD in order to evaluate their crystallinity. Fig. 1 shows the XRD diffractograms for Anatase and Brookite powders. In the Anatase sample (Fig. 1c) the typical main diffraction peak at  $25.28^\circ$  (101) can be observed along with other well-known positions. In Fig. 1a, the two Brookite peaks

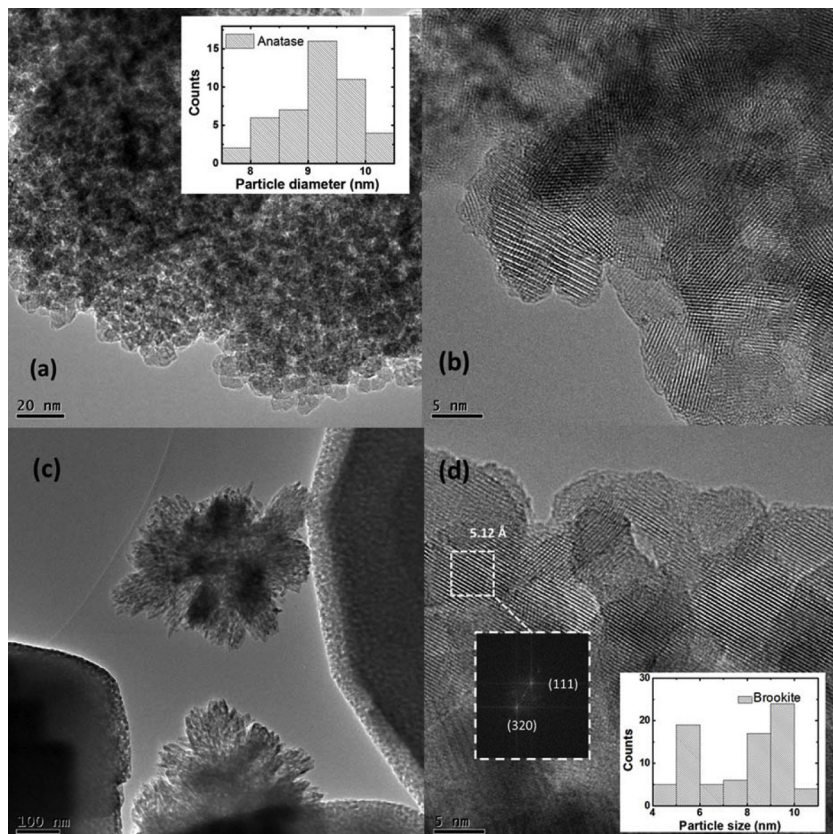


**Fig. 2.** TEM images with different magnification for  $\text{TiO}_2$  (a and b) Anatase and (c and d) Brookite phase showing FFT on selected area.

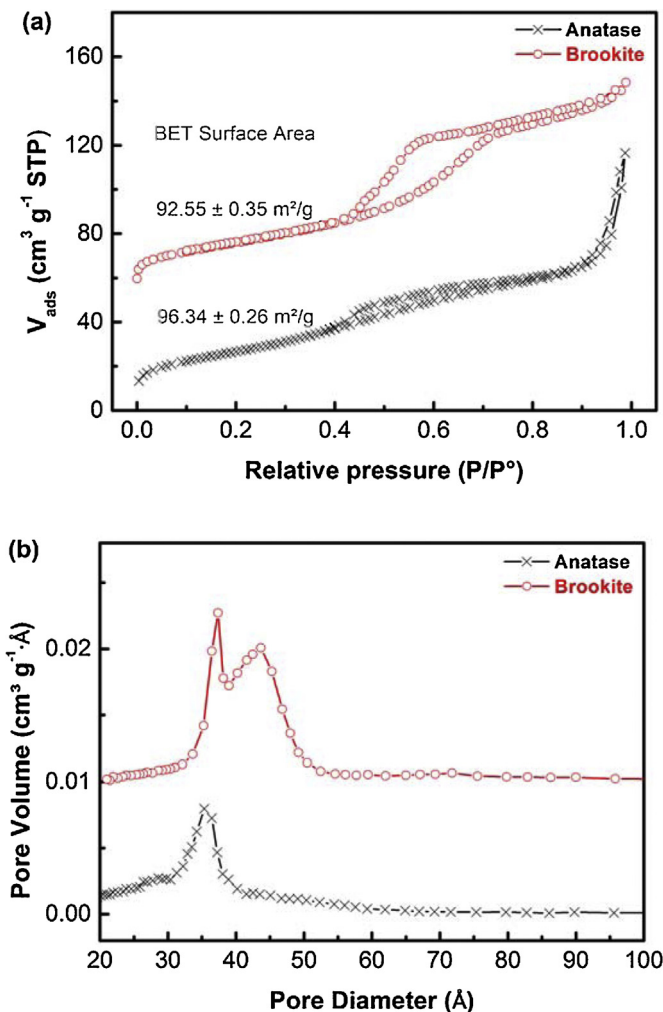


**Fig. 3.** (a) Nitrogen adsorption/desorption isotherms, and (b) pore size radius distributions of  $\text{TiO}_2$  Anatase and Brookite heat-treated at  $400^\circ\text{C}$ .

at  $25.34^\circ$  (120) and  $25.69^\circ$  (111) appear as one peak, along with an intense and sharp peak at  $30.81^\circ$  (121) which is distinctive for such phase. Debye-Scherrer equation was used to determine the crystallite size for each of the samples giving a value of 9.3 and 15.6 nm for Anatase and Brookite, using peaks at  $25.28^\circ$  and  $30.81^\circ$  correspondingly.

TEM images revealed agglomeration in both Anatase and Brookite samples. Anatase seems to be composed of small particles, with a major population of 9.2 nm (Fig. 2a). Brookite is composed by large egg-shell agglomerates with an average value of 1.5  $\mu\text{m}$  long which seems to come from fully-grown star-like nuclei also found in the same sample (Fig. 2c). This is also discussed later with BET measurements. In a more detailed analysis, smaller particles can be observed with two particle size population of 6.0 nm and 9.0 nm. This second average value is in good agreement with the crystallite size calculated by Debye-Scherrer's formula. Electron diffraction patterns were obtained with Fast Fourier Transform (FFT) analysis from selected areas (Fig. 2b and d) that allowed to determine interplanar distances of  $3.78 \text{\AA}$  in the direction (1 0 1) and  $5.12 \text{\AA}$  (320) associated with Anatase and Brookite phases, respectively.

$\text{TiO}_2$  Anatase and Brookite were evaluated by  $\text{N}_2$ -adsorption and results are presented in Fig. 3a. The shape of the nitrogen adsorption/desorption curves is typical of a type-IV isotherm characteristic of mesoporous materials for both  $\text{TiO}_2$  Anatase and Brookite. The BET surface area of Anatase and Brookite  $\text{TiO}_2$  are respectively 96.3 and  $92.5 \text{ m}^2 \text{ g}^{-1}$ , determined by nitrogen adsorp-

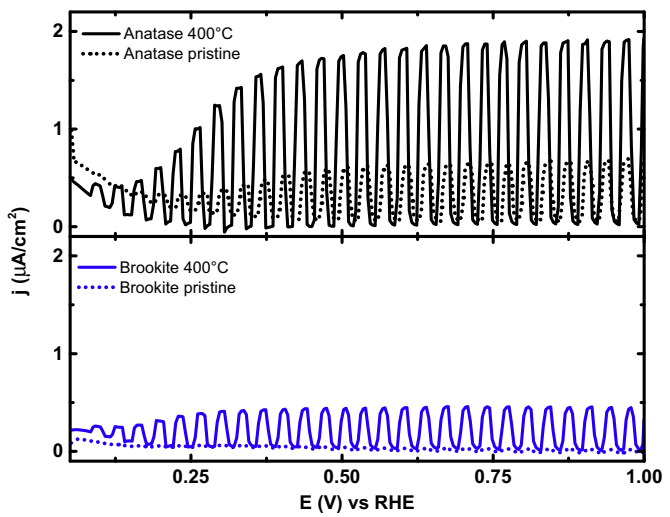


**Fig. 4.** Photocurrent transients (on-off) for  $\text{TiO}_2$  Anatase, and Brookite phases (pristine and  $400^\circ\text{C}$ ) on FTO substrates in a  $0.5 \text{ M H}_2\text{SO}_4$  electrolyte at  $v = 5 \text{ mV/s}$ . A glassy carbon and RHE served as counter, and reference electrode, respectively. Irradiance at electrode =  $5.0 \text{ mW/cm}^2$ .

tion experiments. The pore size distribution of the obtained porous  $\text{TiO}_2$  Anatase and Brookite are shown in Fig. 3b. The pore size distribution in Anatase, with a single peak between 30 and 40 nm, and Brookite with the first peak at between 30 and 40 nm and the second peak at between 40 and 50 nm, is in the range of mesoporous (5–50 nm) materials [34]. It is greatly supported by correlating the pore size distribution with the images of TEM (Fig. 2c) that the first and second range mesoporous in  $\text{TiO}_2$  Brookite for the distribution correspond to the pores within nanoparticles in two different forms of aggregates.

### 3.2. Electrochemical characterization

The electrochemical behavior of the two different phases of  $\text{TiO}_2$  was studied by photocurrent transients and voltammetric measurements. In Fig. 4, the photocurrent transients of the two different  $\text{TiO}_2$  crystalline phases before and after the calcination at  $400^\circ\text{C}$  are shown. As it is observed, the calcination procedure performed on the samples has a positive effect on the magnitude of the photocurrent density ( $j_{\text{ph}}$ ) yielding a higher value. While the initial intention of the calcination was to promote similar surface areas, this procedure has a beneficial effect in terms of the generation of  $e^- - h^+$ , as observed in the Anatase sample, which is a highly desirable feature for  $\text{TiO}_2$  materials. In the case of pristine Brookite, no photocurrent is observed in the transients and can be ascribed to the initial formation of the intermediate compound  $\text{Ti}_2\text{O}_3(\text{H}_2\text{O})_2(\text{C}_2\text{O}_4)\text{-H}_2\text{O}$  at the end of its synthesis [19]. It is only when thermally treated that the crystalline phase is promoted and then charge separation is obtained.

As part of this study, the influence of the amount of suspension deposited in the substrate was also evaluated. This effect can be also regarded as the thickness of the deposited  $\text{TiO}_2$  films. Fig. 5a presents the extracted  $j_{\text{ph}}$  for two photo-electrodes prepared with each of the crystalline phases, denominated as "thick" ( $180 \mu\text{L}$ ,  $15 \text{ mg/ml}$ ,  $1800 \text{ rpm}$ ,  $1.2 \text{ mg}$ ) with 3 times more suspension than that regarded as "thin" ( $60 \mu\text{L}$ ,  $0.4 \text{ mg}$ ), while fixing the substrate area and geometric factor to  $0.49 \text{ cm}^2$  ( $0.7 \text{ cm} \times 0.7 \text{ cm}$ ). Such effect is reflected in the  $j_{\text{ph}}$  obtained with the "thick" sample about 2.5, and 1.5 times higher than the "thin" sample for Brookite and Anatase, respectively.

This difference in the obtained  $j_{\text{ph}}$  at the plateau seems to be associated to a conductivity issue and possibly be related to the

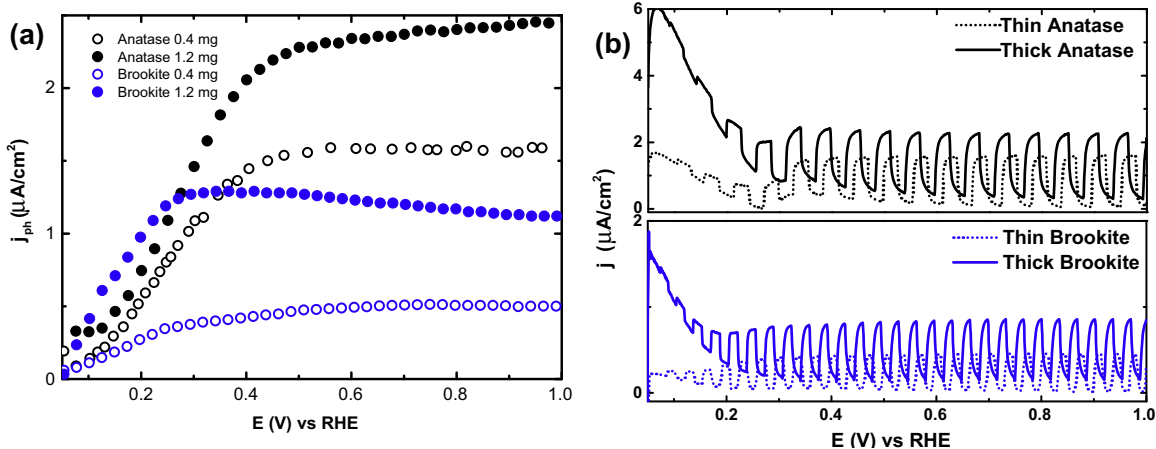


**Fig. 5.** Thickness layer effect. (a) Extracted photocurrent density and (b) photocurrent transients for  $\text{TiO}_2$  Anatase and Brookite phase (as-prepared and heat-treated) on 0.4 mg and 1.2 mg layer electrodes. Experiments were recorded in a 0.5 M  $\text{H}_2\text{SO}_4$ . A glassy carbon, and RHE served as counter and reference electrode, respectively. Irradiance at electrode = 5.0 mW/cm<sup>2</sup>.

morphology, as observed by TEM. To prove this hypothesis, the photocurrent transients were recorded for the Brookite sample (Fig. 5b). It is also noteworthy to point that with the increase in the amount of photocatalyst the capacitive charge at low potential values (close to 0.05 V vs RHE) becomes more significant due to the thickness of the layer. Near 0.2 V and afterwards, this feature is not so noticeable and the photocurrent decay does not occur sufficiently fast to reach the dark current or the  $j_{ph}$  plateau values. This is called photocurrent relaxation and is present in semiconductors exhibiting an exponential decay when photon excitation is suddenly stopped and is dependent of several factors, including the film thickness. Such exponential decay of the photocurrent has the form:

$$j_{ph}(t) = Ae^{-t/\tau} \quad (1)$$

where  $A$  is a constant, and  $\tau$  is the electron collection time [35]. When the charge transport was studied in DSSC  $\text{TiO}_2$  thin films by Solbrand et al. [36] it was found that the thinnest films achieved the highest quantum yield, regardless of the illumination configuration (electrode/electrolyte, EE, or substrate/electrode, SE) and this phenomenon was explained in terms of electron transport losses before the collection at the back contact (ITO surface). Although these observations have shown that larger film thicknesses are not favorable for electron collection injected from an excited dye, our results showed that the generated  $j_{ph}$  is still higher in thicker films. This can be understood as an efficient light penetration distance through the whole film where the electron-hole pair ( $e^- - h^+$ ) separation is generated. However, an important contribution of the capacitive properties plays a role in the development of the transient current. After using Eq. (1) to adjust the photocurrent decay at  $E > 0.6$  V/RHE, a larger  $\tau$  is obtained for the thicker electrode (18% and 15% for Anatase and Brookite, respectively) which demonstrates a longer relaxation. Such parameter suggests that with an increasing film thickness, the current transport faces electron trapping in the bulk of the material and is emphasized in nanoparticulated systems [37]. This is also coherent with the appearance of the capacitance observed in the accumulation region at potential lower than 0.2 V/RHE which have been associated to a chemical capacitance of deep traps [38].

In order to gain a deeper understanding of the dependence of the capacitive properties on the applied potential for these materials, electrochemical impedance spectroscopy measurements were performed. The experiment was performed in 0.5 M  $\text{H}_2\text{SO}_4$  in a wide range of frequencies (50 mHz to 100 kHz) in order to find a

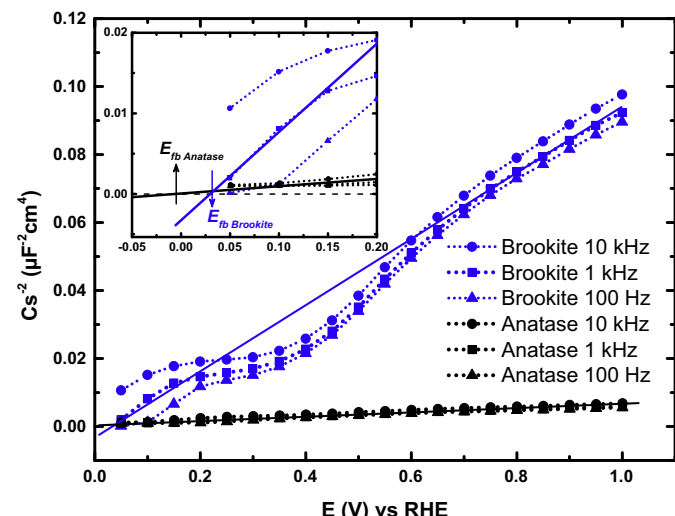


**Fig. 6.** Mott-Schottky plots for Anatase and Brookite electrodes prepared on FTO substrate in 0.5 M  $\text{H}_2\text{SO}_4$ .

**Table 1**  
Summarized  $E_{fb}$  and  $E_g$  values obtained by the corresponding techniques.

Sample	$E_{fb}$ (V)/RHE		$E_g$ (eV)	
	$E_{onset}$	Mott-Schottky	Tauc plot	Diffuse reflectance
Anatase	-0.02	-0.01	3.26	3.30
Brookite	0.02	0.03	3.30	3.36

range in which the capacitance was independent of frequency. For this purpose, it was observed that capacitance remains constant in the medium frequencies range from 100 Hz to 10 kHz and for such reason they were used for these experiments. These values were used to approximate its slope and then extrapolate to zero capacitance for  $E_{fb}$  determination. Assuming that the capacitance of the Helmholtz layer is much bigger than that of the space charge layer ( $C_{sc}$ ), we can calculate the latter and plot its dependence against the applied potential. The corresponding Mott-Schottky plot is shown in Fig. 6 that compares the  $C_{sc}$  behavior for the 2 samples. The flat band potential ( $E_{fb}$ ) can be obtained from extrapolating the slope and the intercept with the potential axis, cf. inset Fig. 6 [39]. The values found are summarized in Table 1. It is interesting to point, that  $E_{fb}$  was more anodic in Brookite than for Anatase, contrary to

what it usually is reported in the literature [40]. These results reveal that the capacitance  $C_{sc}$  of the material seems to be influenced by the surface states, as pointed out by other authors [38]. To verify these observations, the onset potential,  $E_{onset}$ , was determined from both, photocurrent transients and linear sweep voltammetry under darkness and illumination to compare to  $E_{fb}$  since it is an equivalent method for such measurements [41]. In both samples the concordance between these techniques seems to be good confirming the suitability of the methods.

Further information on the spectral response was obtained by two different approaches: action spectra and diffuse reflectance. In the former technique a specific wavelength is irradiated on the sample and currents were recorded while polarizing the electrode at 1.0 V vs RHE. Oliva et al. [42] also suggested that for a crystalline semiconductor the photocurrent density,  $j_{ph}$ , has a dependence to its light absorption response and can be expressed by the following equation:

$$j_{ph} = A \frac{(hv - E_g)^n}{hv} \quad (2)$$

where  $A$  is a constant which depends on the optical transition type,  $n=0.5$  for indirect optical transitions and  $n=2$  for direct optical transitions, and  $E_g$  is the bandgap energy. After applying the light source photo emission correction, the spectra can be transformed into a Tauc plot (inset Fig. 7a) by plotting  $(j_{ph} \times hv)^2$  vs  $hv$ . From this figure, the  $E_g$  can be obtained by the extrapolation of a linear fit near the absorption edge to the energy axis and the value is in well agreement with those reported in the literature [24]. UV-vis diffuse reflectance was performed in order to confirm the results observed by photo-electrochemistry, and the modified Kubelka-Munk method was used to plot the curve  $((K/S) \times hv)^{1/2}$  vs  $hv$  presented in Fig. 7a. In an analog fashion, a tangent line is extrapolated from the slope to the energy axis to obtain the bandgap value. Table 1 summarizes the values obtained by both methods. By accessing the  $E_g$  value and assuming that  $E_{fb}$  and the conduction band ( $E_{cb}$ ) practically merges at the  $E_{onset}$  [43], then we can schematize an energy diagram for the two phases and position the conduction band ( $E_{cb}$ ), and the valence band ( $E_{vb}$ ) (Fig. 7b).

### 3.3. Photo-electrocatalytic activity evaluation

The photocatalytic activity of the semiconductor powders was investigated based on the degradation of the potassium carmine indigo trisulfonate (InC) under UV-vis irradiation. In order to compare with the synthesized samples, commercial Degussa P25 was used as a reference. It is important to remember that the term degradation does not necessarily implies complete mineralization of the organic compound. The photoelectrochemical system used for the degradation comprised an in-house assembled microfluidic device described in Fig. 8a. In brief, the micro-photoelectrochemical reactor is fed with a  $3.5 \times 10^{-4}$  M InC solution in 0.5 M  $K_2SO_4$  through an inlet that conducts to nine microchannels of 700  $\mu m$  wide and deep at a constant flow speed of 12.1 mL with a peristaltic pump. The channels are in direct contact with the photocatalytic materials and irradiated in a SE configuration with a polychromatic light intensity of 34.0 mW/cm<sup>2</sup>. The total volume in the system was 3 mL in each of the experiments. The degradation of the InC was followed by UV-vis spectroscopy at  $\lambda_{max} = 603$  nm. Fig. 8b shows the changes in absorbance for the samples after the treatment performed without (open-circuit potential, OCP) and with an external applied electrode potential (1.0 V/SCE). We observed that the effect of the applied electrode potential significantly decreases the absorbance at the end of the experiment, regardless of the material. Although Anatase and P25 samples showed a higher benefit from the polarization, the Brookite electrode observed the higher

degradation yield, even at OCP condition (in presence of oxygen) in spite that it showed a lower photocurrent generation as observed by the photocurrent transients.

This behavior can be understood in terms of the hole generation since it is well known that when  $e^- - h^+$  pairs are generated; the electron is extracted from the circuit via the substrate (FTO) while the hole travels to the surface of the material at the semiconductor/electrolyte interface where it can directly interact with the dye molecule promoting its oxidation. Later on, when the surface is polarized and the recombination is minimized, the dye degradation is more efficient and is reflected as a lower absorbance value. Such behavior might be explained with the help of the energy diagram (Fig. 7b), in which the valence band (energy level for holes) of Brookite is at a slightly higher energy level than that of the Anatase.

Surface properties are also important to be considered in these experiments. It is usual to find experimental conditions that imply stirring of suspensions where both, the molecule to degrade and the photocatalyst, are moving in a confined volume, which differs from the ones used in this experiment with a static powder and a solution at a constant flow. This represents a change in the dynamics for the adsorption at the material surface, a process that has been previously studied by Mattson et al. for  $TiO_2$  crystalline phases [44]. In their study, they found that acetone had a stronger bonding to Brookite than to Anatase regardless of particle size but sensitive to the contact time. Although the FT-IR spectrum on both crystalline phases had similarities, higher concentration of coordinated species was found on Brookite surface and was reflected in a larger quantum yield in photocatalysis. This is in good agreement with the trend we found in our experiments, with a better degradation performance on Brookite.

To clarify the results obtained by UV-vis spectroscopy, Raman spectra (RS) of the solutions were recorded and shown in Fig. 9a. A copper plate was used as substrate to support the solutions and its spectrum was also recorded. The spectral assignments considered in the recorded RS are in the range of 2000–200  $cm^{-1}$  and are as follows: C=C–CO–C bending 547  $cm^{-1}$ , C–NH–C bending 575  $cm^{-1}$ ,  $-SO_3^-$  bending 618  $cm^{-1}$ , C–N–C bending 722  $cm^{-1}$ , C–C, C=O out of plane bending and C–S stretching 819  $cm^{-1}$ ,  $-S-O$  stretching deformation 978  $cm^{-1}$ ,  $-SO_2$  and C=C stretching 1130  $cm^{-1}$ , N–C stretching 1185  $cm^{-1}$ ,  $-SO_3$  stretching 1293  $cm^{-1}$ , N=C=C–N stretching 1444  $cm^{-1}$ , C=C stretching 1539  $cm^{-1}$ , C=C and C=O stretching at 1581 and 1632  $cm^{-1}$  [45–48]. Fig. 9a shows the individual spectrum for the Cu plate, supporting electrolyte and InC. We observed that some of the features related to the Cu plate are still visible in the spectra of the  $K_2SO_4$  and InC for wavenumbers smaller than 700  $cm^{-1}$ . The band at 976  $cm^{-1}$  can be attributed to the stretching vibration of  $-SO_4^{2-}$  coming from the supporting electrolyte. The signals at 819, 1130, 1184, 1295, 1539 and 1580  $cm^{-1}$  are attributed to the vibrational modes of the InC and are in agreement with both theoretical and experimental approximations done by other authors [45]. There is a broadening of the spectra in the region from 1800 to 1100  $cm^{-1}$  due to the substrate as it can be observed for the solution treated at OCP condition with the P25 sample (Fig. 9b). The same figure shows that, most of the bands assigned to InC decrease their intensity after the photoelectrochemical treatment even at OCP condition and when a potential bias is applied they are almost not observable. However, the solutions still have a very light blue color at the end of the experiments which can be explained by the presence of the chromophore part of the InC, especially the bands at 547 and 575  $cm^{-1}$  assigned to the bending vibrations of C=C–CO–C group. However, the signals from the Cu plate appearing at the same wavenumbers account with the determination of such bands and, therefore, cannot be distinguished due to the low concentration.

Indigo carmine compounds decomposition is certainly complex, and the determining factors for this process depend on the working

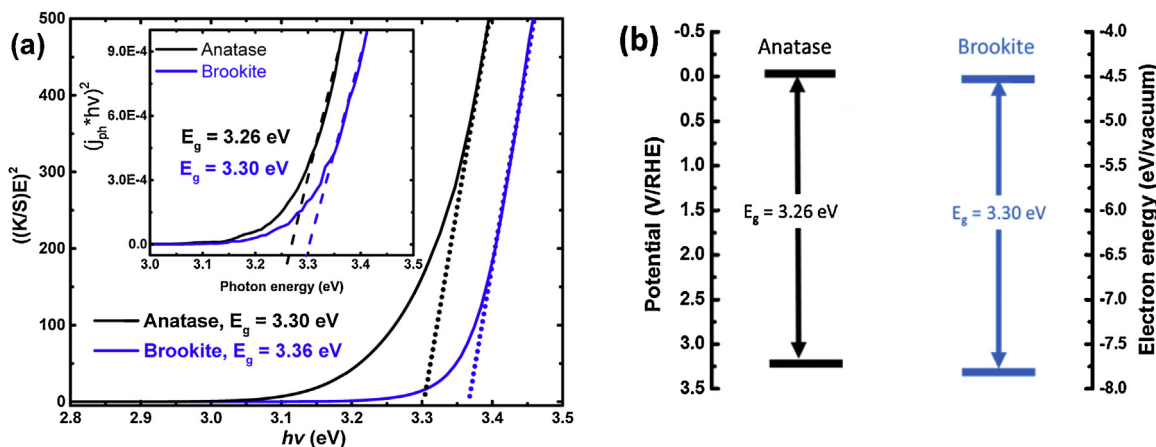


**Fig. 7.** (a) Kubelka-Munk vs photon energy plot for Anatase (400 °C), and Brookite (400 °C) obtained by diffuse reflectance. A glassy carbon, and RHE served as counter and reference electrodes, respectively. Irradiance at electrode distance = 5.0 mW/cm<sup>2</sup>. (b) Relative Energy positions for Anatase and Brookite with data from electrochemical experiments.

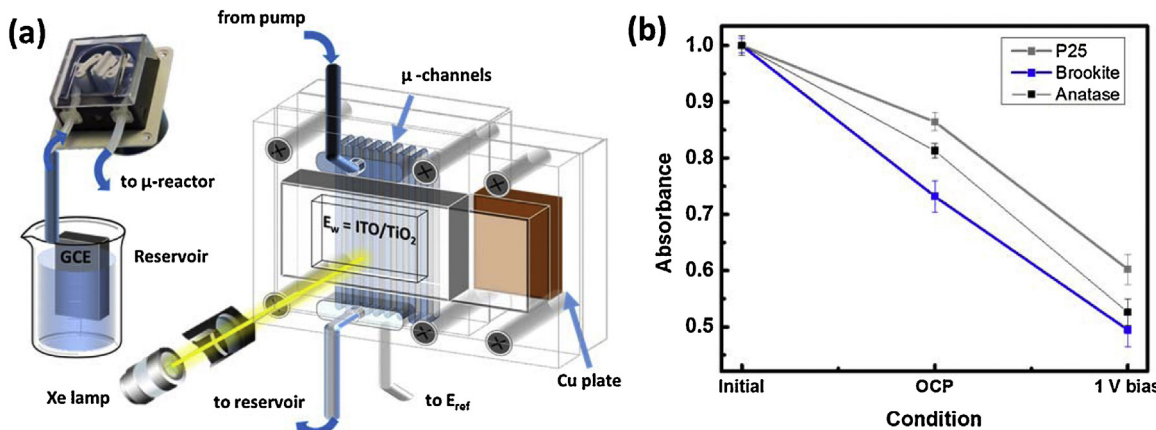


**Fig. 8.** (a) Micro-fluidic photo electrochemical reactor scheme used for the dye degradation. (b) Absorbance for indigo carmine solution ( $3.5 \times 10^{-4}$  M) after 180 min of treatment in the micro-reactor in a solution containing 0.5 M K<sub>2</sub>SO<sub>4</sub>.

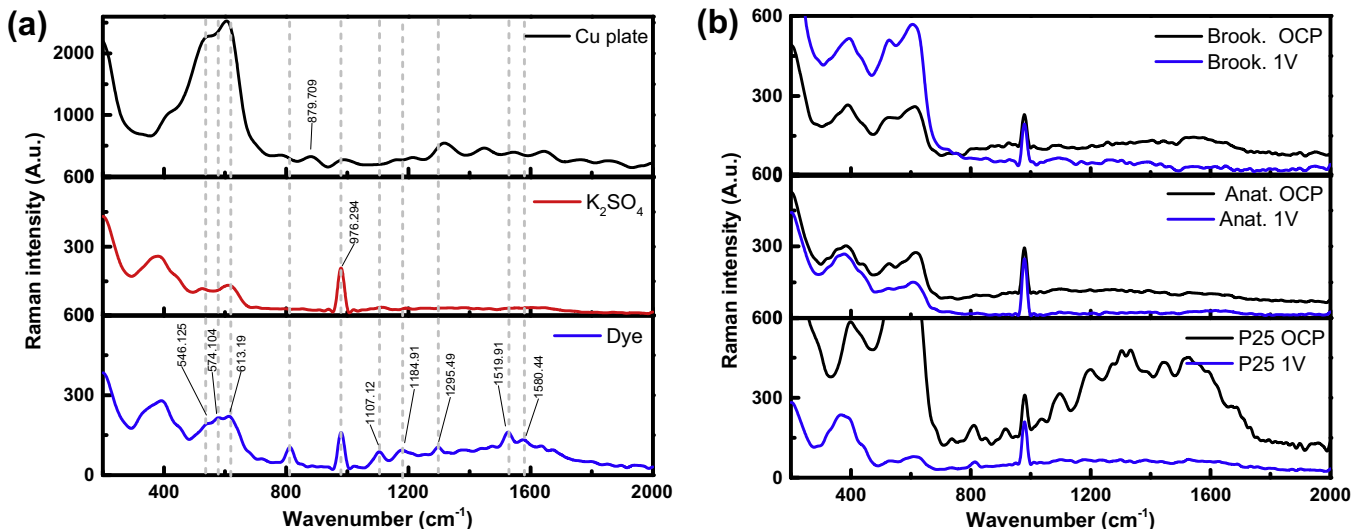


**Fig. 9.** (a) Raman spectra obtained for the substrate (Cu plate), supporting electrolyte (0.5 M K<sub>2</sub>SO<sub>4</sub>) and the indigo carmine ( $3.5 \times 10^{-4}$  M). (b) Raman spectra recorded for oxidized solutions after exposition to TiO<sub>2</sub> samples after an irradiation power of 3.4 mW/cm<sup>2</sup> for 180 min. The Raman laser power was 4.5 mW (780 nm) and reading was averaged from 200 acquisitions.

conditions of the selected method. While photocatalysis of these compounds depends strongly on the band positions and surface

energy adsorption, and on the catalyst polymorph; the electrochemical treatments are also importantly influenced by pH and

ion type present in the electrolyte. When these degradation methods are compared, electrochemical approaches have demonstrated superior performance when chlorinated species are in the solution but the reaction yield decreases with the presence of sulfate ions [49]. Our study represents a combination of these methods and faces the complexity of both. While sulfate ions are present and represent a setback for the decomposition rate of the InC, an important degree of degradation was accomplished with the photocatalytic approach, i.e., at OCP condition, and even further via the photo-electrocatalytic approach at 1 V/SCE. Taking in account these situations and the fact that Brookite sample exhibited a higher degradation rate, it can be confirmed that crystalline phase in TiO<sub>2</sub> is a very important factor to be considered for water treatment applications. However, further experimentation is indeed required to optimize the conditions for these kind of devices that represent an interesting design for studying small volumes but also can be projected to an upscale application.

#### 4. Conclusions

In this work, the photo-electrochemical properties of TiO<sub>2</sub> Brookite and Anatase polymorphs obtained by chemical thermolysis from titanium oxysulfate with and without anionic species were investigated. XRD diffractograms showed that preferential planes (3 2 0) and (1 1 1) for brookite and (1 0 1) for Anatase were obtained after a thermal treatment (400 °C, under air) as observed by FFT in TEM images. Differences in the morphology and particle size were found in these images suggesting unlike electrochemical behavior as confirmed in the photocurrent transients performed in 0.5 M H<sub>2</sub>SO<sub>4</sub>. These curves revealed that the best material for e<sup>-</sup>-h<sup>+</sup> pair photogeneration was the Anatase phase. The amount of catalyst material in the photo-electrodes was also evaluated and was found that with increasing deposited mass the j<sub>ph</sub> is enhanced although with transport losses as it was observed by the increase of the apparent capacitance and in the relaxation process from the photocurrent transient curves. This was partially supported by Mott-Schottky analysis which shows different capacitance properties for the two photocatalysts suggesting kinetic differences in the electron pathway. Diffuse reflectance spectroscopy and Tauc plots were used to determine E<sub>g</sub> and Mott-Schottky plot to obtain E<sub>fb</sub> for each material. Finally, the photocatalytic activity of these samples was evaluated in the degradation of InC using a home-made photo-electrochemical microreactor. The treated solutions were assessed by UV-vis and Raman spectroscopy and it was found that Brookite sample was the most efficient photocatalyst in both OCP and polarized conditions. This phenomenon was understood as a consequence of the energy level for the valence band of Brookite which has a higher oxidizing power than the Anatase.

#### Acknowledgments

J.A. Díaz-Real thanks the National Council for Science and Technology of México (CONACyT) for financial support through scholarships No. 242857 and the University de Poitiers for use of infrastructure, equipment and facilities used in the doctoral stage.

#### Appendix A. Supplementary data

Supplementary data associated with this article can be found, in the online version, at <http://dx.doi.org/10.1016/j.apcatb.2016.06.008>.

#### References

- [1] A. Kar, Y.R. Smith, V. Subramanian, Improved photocatalytic degradation of textile dye using titanium dioxide nanotubes formed over titanium wires, Environ. Sci. Technol. 43 (2009) 3260–3265.
- [2] M.J. López-Muñoz, A. Revilla, G. Alcalde, Brookite TiO<sub>2</sub>-based materials: synthesis and photocatalytic performance in oxidation of methyl orange and As(III) in aqueous suspensions, Catal. Today 240 (Part A) (2015) 138–145.
- [3] A. Di Paola, M. Bellardita, L. Palmisano, Brookite, the least known TiO<sub>2</sub> photocatalyst, Catalysts 3 (2013) 36.
- [4] O. Glemser, E. Schwarzmann, Zur polymorphie des titandioxyds, Angew. Chem. 68 (1956) 791.
- [5] K. Noll, Zur Bildung von Brookit, Naturwissenschaften 48 (1961) 601.
- [6] S. Yamaguchi, Brookite film on titanium, J. Electrochem. Soc. 108 (1961) 302.
- [7] M. Kobayashi, V. Petrykin, K. Tomita, M. Kakihana, Hydrothermal synthesis of brookite-type titanium dioxide with snowflake-like nanostructures using a water-soluble citratoperoxotitanate complex, J. Cryst. Growth 337 (2011) 30–37.
- [8] M. Kiyama, T. Akita, Y. Tsutsumi, T. Takada, Formation of titanite oxides of anatase, brookite and rutile types by aerial oxidation of titanous solutions, Chem. Lett. 1 (1972) 21–24.
- [9] T. Oota, I. Yamai, H. Saito, Brookite formation by the oxidation of titanium metal under hydrothermal conditions, J. Ceram. Assoc. Japan 87 (1979) 375–382.
- [10] T. Mitsuhashi, M. Watanabe, Brookite formation from precipitates containing calcium ions, Mineral. J. 9 (1978) 236–240.
- [11] P. Arnal, R.J.P. Corriu, D. Leclercq, P.H. Mutin, A. Vioux, Preparation of anatase, brookite and rutile at low temperature by non-hydrolytic sol-gel methods, J. Mater. Chem. 6 (1996) 1925–1932.
- [12] B. Zhao, F. Chen, Q. Huang, J. Zhang, Brookite TiO<sub>2</sub> nanoflowers, Chem. Commun. (2009) 5115–5117.
- [13] L. Zhang, V.M. Menendez-Flores, N. Murakami, T. Ohno, Improvement of photocatalytic activity of brookite titanium dioxide nanorods by surface modification using chemical etching, Appl. Surf. Sci. 258 (2012) 5803–5809.
- [14] B.L. Bischoff, M.A. Anderson, Peptization process in the sol-gel preparation of porous anatase (TiO<sub>2</sub>), Chem. Mater. 7 (1995) 1772–1778.
- [15] S. Musić, M. Gotić, M. Ivanda, S. Popović, A. Turković, R. Trojko, A. Sekulić, K. Furić, Chemical and micro structural properties of TiO<sub>2</sub> synthesized by sol-gel procedure, Mater. Sci. Eng. B 47 (1997) 33–40.
- [16] B.A. Morales, O. Novaro, T. López, E. Sánchez, R. Gómez, Effect of hydrolysis catalyst on the Ti deficiency and crystallite size of sol-gel-TiO<sub>2</sub> crystalline phases, J. Mater. Res. 10 (1995) 2788–2796.
- [17] A. Pottier, C. Chaneac, E. Tronc, L. Mazerolles, J.-P. Jolivet, Synthesis of brookite TiO nanoparticles by thermolysis of TiCl<sub>4</sub> in strongly acidic aqueous media, J. Mater. Chem. 11 (2001) 1116–1121.
- [18] S.R. Hall, V.M. Swinerd, F.N. Newby, A.M. Collins, S. Mann, Fabrication of porous titania (brookite) microparticles with complex morphology by sol-gel replication of pollen grains, Chem. Mater. 18 (2006) 598–600.
- [19] D. Dambournet, I. Belharouak, J. Ma, K. Amine, Toward high surface area TiO<sub>2</sub> brookite with morphology control, J. Mater. Chem. 21 (2011) 3085–3090.
- [20] D. Dambournet, I. Belharouak, K. Amine, Tailored preparation methods of TiO<sub>2</sub> anatase, rutile, brookite: mechanism of formation and electrochemical properties, Chem. Mater. 22 (2010) 1173–1179.
- [21] T.A. Kandiel, A. Feldhoff, L. Robben, R. Dillert, D.W. Bahnemann, Tailored titanium dioxide nanomaterials: anatase nanoparticles and brookite nanorods as highly active photocatalysts, Chem. Mater. 22 (2010) 2050–2060.
- [22] S. Bakardjieva, V. Stengl, L. Szatmáry, J. Subrt, J. Lukac, N. Murafa, D. Niznansky, K. Cizek, J. Jirkovsky, N. Petrova, Transformation of brookite-type TiO<sub>2</sub> nanocrystals to rutile: correlation between microstructure and photoactivity, J. Mater. Chem. 16 (2006) 1709–1716.
- [23] B. Zhao, F. Chen, Y. Jiao, J. Zhang, Phase transition and morphological evolution of titania/titanate nanomaterials under alkalescent hydrothermal treatment, J. Mater. Chem. 20 (2010) 7990–7997.
- [24] M. Landmann, E. Rauls, W.G. Schmidt, The electronic structure and optical response of rutile, anatase and brookite TiO<sub>2</sub>, J. Phys. Condens. Matter 24 (2012) 195503.
- [25] C. Magne, F. Dufour, F. Labat, G. Lancel, O. Durupthy, S. Cassaignon, T. Pauperté, Effects of TiO<sub>2</sub> nanoparticle polymorphism on dye-sensitized solar cell photovoltaic properties, J. Photochem. Photobiol. A Chem. 232 (2012) 22–31.
- [26] B.I. Lee, S. Kaewgun, W. Kim, W. Choi, J.S. Lee, E. Kim, Visible light photocatalytic properties of polymorphic brookite titania, J. Renewable Sustainable Energy 1 (2009) 023101.
- [27] B. Ohtani, J. Kawaguchi, M. Kozawa, Y. Nakaoka, Y. Nosaka, S. Nishimoto, Effect of platinum loading on the photocatalytic activity of cadmium(II) sulfide particles suspended in aqueous amino acid solutions, J. Photochem. Photobiol. A Chem. 90 (1995) 75–80.
- [28] J.-G. Li, C. Tang, D. Li, H. Haneda, T. Ishigaki, Monodispersed spherical particles of brookite-type TiO<sub>2</sub>: synthesis, characterization, and photocatalytic property, J. Am. Ceram. Soc. 87 (2004) 1358–1361.
- [29] J. Xie, X. Lü, J. Liu, H. Shu, Brookite titania photocatalytic nanomaterials: synthesis, properties, and applications, Pure Appl. Chem. 81 (2009) 2407–2415.

[30] X. Shen, J. Zhang, B. Tian, M. Anpo, Tartaric acid-assisted preparation and photocatalytic performance of titania nanoparticles with controllable phases of anatase and brookite, *J. Mater. Sci.* 47 (2012) 5743–5751.

[31] Z. Li-Jun, Y.A.N. Shan-Shan, T. Bao-Zhu, C. Feng, Z. Jin-Long, H. Jia-Zhen, Preparation and characterization of anatase-brookite  $\text{TiO}_2$  film on the PET surface, *Acta Phys. Chim. Sin.* 22 (2006) 569.

[32] F. Iskandar, A.B.D. Nandyanto, K.M. Yun, C.J. Hogan, K. Okuyama, P. Biswas, Enhanced photocatalytic performance of brookite  $\text{TiO}_2$  macroporous particles prepared by spray drying with colloidal templating, *Adv. Mater.* 19 (2007) 1408–1412.

[33] J.e. Shi, S. Shang, L. Yang, J. Yan, Morphology and crystalline phase-controllable synthesis of  $\text{TiO}_2$  and their morphology-dependent photocatalytic properties, *J. Alloys Compd.* 479 (2009) 436–439.

[34] C.J.H. Jacobsen, C. Madsen, J. Houzvicka, I. Schmidt, A. Carlsson, Mesoporous zeolite single crystals, *J. Am. Chem. Soc.* 122 (2000) 7116–7117.

[35] J. van de Lagemaat, A.J. Frank, Nonthermalized electron transport in dye-sensitized nanocrystalline  $\text{TiO}_2$  films: transient photocurrent and random-walk modeling studies, *J. Phys. Chem. B* 105 (2001) 11194–11205.

[36] A. Solbrand, A. Henningsson, S. Södergren, H. Lindström, A. Hagfeldt, S.-E. Lindquist, Charge transport properties in dye-sensitized nanostructured  $\text{TiO}_2$  thin film electrodes studied by photoinduced current transients, *J. Phys. Chem. B* 103 (1999) 1078–1083.

[37] C. Wehrenfennig, C.M. Palumbiny, H.J. Snaith, M.B. Johnston, L. Schmidt-Mende, L.M. Herz, Fast charge-carrier trapping in  $\text{TiO}_2$  nanotubes, *J. Phys. Chem. C* 119 (2015) 9159–9168.

[38] L. Bertoluzzi, I. Herráiz-Cardona, R. Gottesman, A. Zaban, J. Bisquert, Relaxation of electron carriers in the density of states of nanocrystalline  $\text{TiO}_2$ , *J. Phys. Chem. Lett.* 5 (2014) 689–694.

[39] K. Gelberman, L. Lee, S.W. Donne, Flat-band potential of a semiconductor: using the Mott-Schottky equation, *J. Chem. Educ.* 84 (2007) 685.

[40] A. Di Paola, M. Bellardita, R. Ceccato, L. Palmisano, F. Parrino, Highly active photocatalytic  $\text{TiO}_2$  powders obtained by thermohydrolysis of  $\text{TiCl}_4$  in water, *J. Phys. Chem. C* 113 (2009) 15166–15174.

[41] H.R. Sprunk, R. Schumacher, R.N. Schindler, Evaluation of the flat-band potentials by measurements of anodic/cathodic photocurrent transitions, *Faraday Discuss. Chem. Soc.* 70 (1980) 55–66.

[42] F.Y. Oliva, La.B. Avalle, E. Santos, O.R. Cámaras, Photoelectrochemical characterization of nanocrystalline  $\text{TiO}_2$  films on titanium substrates, *J. Photochem. Photobiol. A Chem.* 146 (2002) 175–188.

[43] R. Beranek, (Photo)electrochemical methods for the determination of the band edge positions of  $\text{TiO}_2$ -based nanomaterials, *Adv. Phys. Chem.* 2011 (2011) 20.

[44] A. Mattsson, L. Österlund, Adsorption and photoinduced decomposition of acetone and acetic acid on anatase, brookite, and rutile  $\text{TiO}_2$  nanoparticles, *J. Phys. Chem. C* 114 (2010) 14121–14132.

[45] N. Peica, W. Kiefer, Characterization of indigo carmine with surface-enhanced resonance Raman spectroscopy (SERRS) using silver colloids and island films, and theoretical calculations, *J. Raman Spectrosc.* 39 (2008) 47–60.

[46] J. Seixas de Melo, R. Rondão, H.D. Burrows, M.J. Melo, S. Navaratnam, R. Edge, G. Voss, Photophysics of an indigo derivative (Keto and Leuco structures) with singular properties, *J. Phys. Chem. A* 110 (2006) 13653–13661.

[47] I.T. Shadi, B.Z. Chowdhry, M.J. Snowden, R. Withnall, Analysis of the conversion of indigo into indigo carmine dye using SERRS, *Chem. Commun.* (2004) 1436–1437.

[48] I.T. Shadi, B.Z. Chowdhry, M.J. Snowden, R. Withnall, Semi-quantitative analysis of indigo carmine using silver colloids, by surface enhanced resonance Raman spectroscopy (SERRS), *Spectrochim. Acta A Mol. Biomol. Spectrosc.* 59 (2003) 2201–2206.

[49] R.E. Palma-Goyes, J. Silva-Agredo, I. González, R.A. Torres-Palma, Comparative degradation of indigo carmine by electrochemical oxidation and advanced oxidation processes, *Electrochim. Acta* 140 (2014) 427–433.